

Full Paper

Influence of laser beam's image-plane position on geometry of through-holes in percussion-drilled glass using excimer laser

Ales Babnik*, Rok Petkovsek and Janez Mozina

University of Ljubljana, Faculty of Mechanical Engineering, Askerceva 6, SI-1000 Ljubljana, Slovenia

*Corresponding author, e-mail: ales.babnik@fs.uni-lj.si

Received: 19 August 2011 / Accepted: 22 January 2013 / Published: 25 January 2013

Abstract: We study the influence of a laser beam's image-plane position relative to the processed surface for the deep-hole, laser-microdrilling of soda-lime glass with an excimer 308-nm laser and mask-projection technique. It is demonstrated that the image-plane position has a significant influence on the hole's tapering and final depth. Holes with exit diameters up to 10 times smaller than the mask-image diameter are produced in the case of perforation during the appropriate process phase determined by the formation of the plasma plume.

Keywords: laser processing, excimer laser, mask-projection technique, glass micro-drilling, hole geometry

INTRODUCTION

Lasers with wavelengths in the UV region are convenient for processing different types of glass due to their high absorption coefficient. Percussion laser drilling is a method for the production of holes with diameter in the micrometre range [1, 2]. For this purpose a small focal diameter beam is needed, which can only be achieved using a high-quality, laser-beam source. Since the beam quality of the excimer laser is rather poor, a single-lens focusing scheme on its own cannot be used [3]. Instead, a special beam treatment should be used to achieve the required properties of the processing beam. Beam homogenisation in combination with a mask-projection technique is a well-known procedure for the processing treatment of the beam [4]. Such an optical system in combination with an excimer laser source is a useful tool for the production of precisely defined holes with diameter down to a few micrometres. However, the hole's definition is only maintained for a low aspect ratio (shallow hole depth compared to diameter). In this case, the physical properties of the laser light (energy and pulse duration) are predominant. The same processing system can also be used for

drilling deep holes with a high aspect ratio when the geometrical properties (focus location and numerical aperture) are as important as the physical properties of the processing beam.

High-aspect-ratio holes drilled with a laser are tapered in most cases. The amount of deviation from the cylindrical shape primarily depends on the geometrical properties of the processing beam. Nearly cylindrical holes can be drilled using a high-quality beam (Gaussian intensity distribution) and a focusing system with a low numerical aperture (NA) [5]. The same processing conditions cannot be achieved when a mask-projection technique is used [2, 6]. Here, the beam diameter at the image plane is defined by the optical system's demagnification and the circular-aperture-mask diameter. It is to be expected that decreasing the image diameter reduces the deep-hole drilling efficiency due to an increase in NA of the focusing optics, which leads to an increased light absorption on the hole's wall. It should be noted that the intensity distribution at the processing point is a flat (top-hat) intensity profile. Consequently, it is probable that the shape of the hole becomes extremely conical or even horn-shaped and the hole's aspect ratio is expected to be small [6]. This deviation from the ideal cylindrical geometry can be prevented by both reducing the NA of the objective lens and properly adjusting the beam's processing point (i.e. mask image or focal point position) with respect to the sample surface. When considering the geometry of the laser micro-drilled hole, two further phenomena occurring inside the microhole need to be considered, i.e. refocusing [7, 8] and the wave-guide effect [9, 10]. These effects may maintain a high light intensity inside the hole, which leads to a cylindrically shaped microhole with a high aspect ratio. So a prediction of the maximum hole depth, calculated with respect to the beam-intensity reduction due to an increase of the beam radius while the beam penetrates into the bulk [11], cannot be confirmed in practice. An interesting calculation was also presented by Paterson et al. [12]. They showed that the hole's taper depends on the energy of the laser beam in such a way that the taper angle can even be negative, i.e. the hole's diameter increases with depth, at higher energy. However, their experiments were performed on a photoresist material and not on a glass-like material. Another model was presented by Tokarev et al. [1], who showed a similar hole-geometry behaviour at processing fluence up to 6 times higher than the threshold fluence. Their model was tested on polymers employed as the processing material. The results of a test ablation of polyimide with regard to the image-plane shift were presented by Gerlach et al. [4].

In general, laser-percussion deep microdrilling is characterised by three process phases according to the three different types of plasma-plume formation when the processing beam with a fluence higher than the threshold value is used. The three phases are related to the removal rate or the hole depth versus the laser pulse number [13, 14] and in a special situation can be clearly visible in the hole's cross section [9]. Knowledge of the beam-material interaction including the plasma formation in each of the three phases is helpful when through holes with the desired exit diameter are processed. Typically, perforation during the second phase results in an exit diameter slightly smaller than the beam focus diameter. When an exit hole diameter much smaller than the focus diameter is required, perforation should be performed during the third process phase. By using this approach an exit hole with a very small diameter, several times smaller than the focus diameter of the beam, can be achieved. Expertise in the production of small-diameter holes is important for some specific applications [6].

So far, research in the laser drilling of high-aspect-ratio holes was devoted mainly to process efficiency, viz. maximisation of the removal rate and the final depth of the hole. Only a few papers

deal with an investigation of deep hole's geometry when processed with a mask-projection system, but none of them deals with the processing of glass material. In this paper we characterise the influence of the high-fluence beam's image-plane position relative to the sample surface on the hole's geometry in percussion-drilled glass. We present the results of some typical combinations of the pulse energy and the NA of the objective-lenses assembly.

EXPERIMENTAL SET-UP

A scheme of our experimental set-up for the mask-projection drilling technique is shown in Figure 1. For the processing laser-beam source, an excimer laser is used with the following characteristics: wavelength $\lambda = 308$ nm, pulse duration = 20 ns, repetition rate = 20 Hz and beam energy up to 100 mJ. The excimer laser is a typical source with a low-quality beam. In our case, a beam with a rectangular profile (5 x 40 mm) and non-uniform beam intensity is emitted from the source. Therefore, a special treatment—homogenisation and spatial filtering—is involved to improve the beam quality at the processing point.

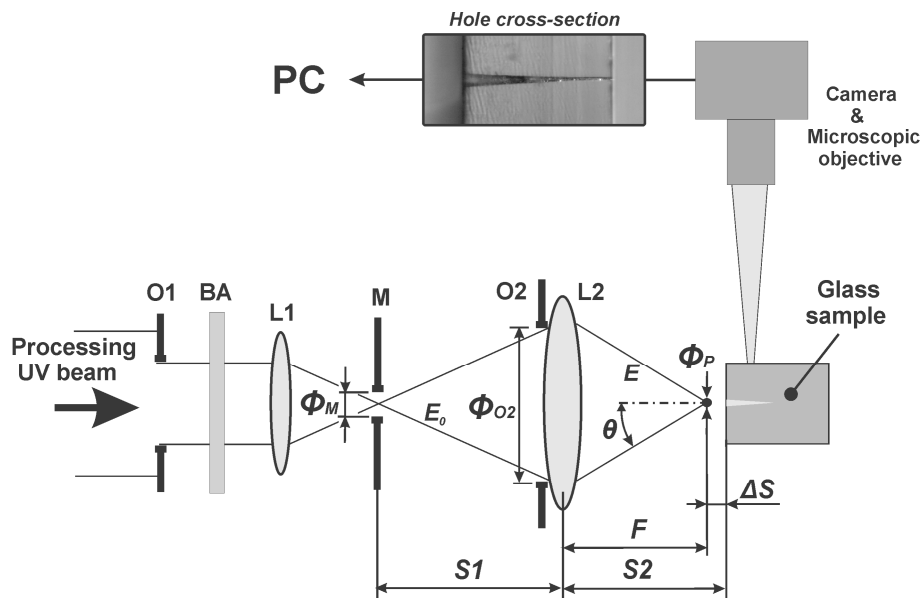


Figure 1. The experimental set-up: O1 and O2 = circular apertures, L1 = focusing lens, L2 = objective assembly, BA = beam attenuator, M = mask, $S1$ = distance from mask to objective lenses, $S2$ = distance between L2 and sample, F = image-plane distance, ΔS = image-plane position shift, Φ_M = mask diameter, Φ_{O2} = adjustable objective aperture diameter, Φ_P = image-plane beam diameter. E_0 and E denote beam energy in front of and after aperture O2

The optical set-up is divided into two sections. The aim of the first section is to homogenise the processing beam. This section consists of a cylindrical beam expander: Kepler telescope (not shown in Figure 1), a circular aperture O1, a focusing lens L1 and a pinhole M. With this optical system, a laser beam with a rectangular profile is expanded in the narrower direction to give a square beam profile. Furthermore, the beam is spatially limited and spatially filtered by focusing through the pinhole. The same pinhole is employed as a mask in the second section. An objective lens system L2 projects the image of the mask M onto the sample surface. With a 1-mm mask diameter Φ_M and an objective magnification of 1/20 (distance $S1/F$ ratio, where $S1 = 400$ mm and $F = 20$ mm), a beam

diameter \varnothing_p of approximately 60 μm is achieved at the image plane (F). Since the projection technique is used, where the laser beam is first focused through the pinhole M and then directed through the objective optics, the focus location coincides with the image plane at the processing point. A similar beam-treatment system has already been used by Buerhop et al. [15] because it successfully improves the beam quality without using an expensive optical homogeniser. It should be noted that in ordinary projection systems the focus position does not coincide with the position of the image [1]. In our case the beam has an almost uniform intensity profile (top-hat profile) at the place of the image, while the intensity profile at the focus has a nearly Gaussian shape. A circular aperture O2 with an adjustable diameter \varnothing_{O2} is used as an iris to control the diameter of the beam passing through the objective lens. In this way we define the NA of the processing beam, which can be expressed as $\text{NA} = \sin \theta$, where θ is the angle of the outermost ray in the focused beam.

By reducing the O2 diameter, not only is the NA adjusted but also the processing energy is changed. To compare some test results the increase in the processing energy due to an enlargement of the O2 diameter is corrected by inserting an appropriate attenuator BA into the beam path.

The processing laser-pulse energy E is varied between 0.2-4.7 mJ by the BA attenuation and O2 diameter adjustment. The beam attenuator is placed between the aperture O1 and the lens L1 to keep the beam's geometrical properties unaffected. The values of E are measured on the exiting side of the objective optics L2 with a calibrated bolometer (Gentec SOLO). Using these data we obtain a beam fluence in the range of 7-165 J/cm^2 (beam intensity: 0.34-8 GW/cm^2) at the image plane.

Plain soda-lime glass samples with a thickness of 0.7 mm are mounted normal to the incident processing beam on the translation stage in order to shift the surface distance $S2$ by the distance ΔS relative to the image-plane distance F . Through the fluorescence of the glass due to UV beam excitation, the image plane location where the laser beam is narrower, can be precisely located within the glass. Knowing the image-plane position in the glass, the image-plane position in the air F can be calculated by taking into account the refractive index of the glass. The experimentally determined ablation threshold was 0.2 mJ and the calculated threshold fluence was $\approx 3.5 \text{ J}/\text{cm}^2$. All the experiments were performed without gas assistance.

The drilling was performed near the sample's upper edge, which was polished to enable real-time, hole-growth observation and imaging of the hole's final cross section. For this purpose, a PC-controlled digital video BW camera, mounted on a microscope objective with a magnification of 110, was used.

OSLO-EDU (Lambda Research) software for optics design and optimisation was used to model the assembly of the L2 objective lenses. The objective construction is shown in Figure 2, where the ray traces are also shown for the largest diameter of aperture O2 used in our experiments.

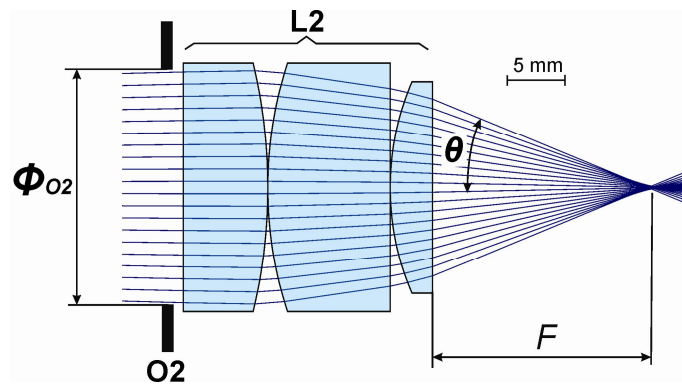


Figure 2. Objective lenses assembly

RESULTS AND DISCUSSION

Drilling tests were performed to analyse the effect of the image-plane position on the hole's geometry at process energy up to 10 times higher than the ablating threshold energy. Experiments were performed at five different combinations of pulse-energy/NA that lead to the most interesting results, presented in Figure 3, where the subfigure columns marked with letters from a) to e) show the drilling results for selected pulse-energy/NA combinations. The image-plane position was shifted along the beam axis (ΔS in Figure 1) with a step of 0.1 mm by moving the sample towards or away from the objective lens. The corresponding plane position shift is marked on each subfigure. During the drilling process, the sample remained at rest. The reference snap-shots, marked with $\Delta S = 0$, denote the sample position where the locus of the image plane coincides with the sample's front surface. Snapshots placed above and under the reference ones in each column show holes processed with the image plane shifted away from the sample's surface and into the bulk respectively. Each drilling test was completed when the hole's growth stopped or the sample was perforated.

The three characteristic drilling phases can be discerned in the photographs of the holes' cross sections. Each phase is associated with a unique hole shape as a consequence of the plasma expansion.

A horn-shaped hole is typical for the first phase when the surface ablation takes place. Ablation in the bulk material in the shape of a half-sphere appears and a cracked-material region is manifested at the place of the laser beam's interaction due to reduced heat transfer and consequent temperature increase. The diameter of this region is large compared to the beam diameter and the ablation rate is much higher in this first phase than in the subsequent phases. Also, it should be noted that the fluence at the processing point is several times higher than the threshold value. By analysing the sample-hole geometry, we can conclude that the taper and the initial diameter of the hole depend heavily on the image-plane position. When the image plane coincides with the sample's front surface, these two properties are at a minimum and increase as the image plane is shifted in both directions.

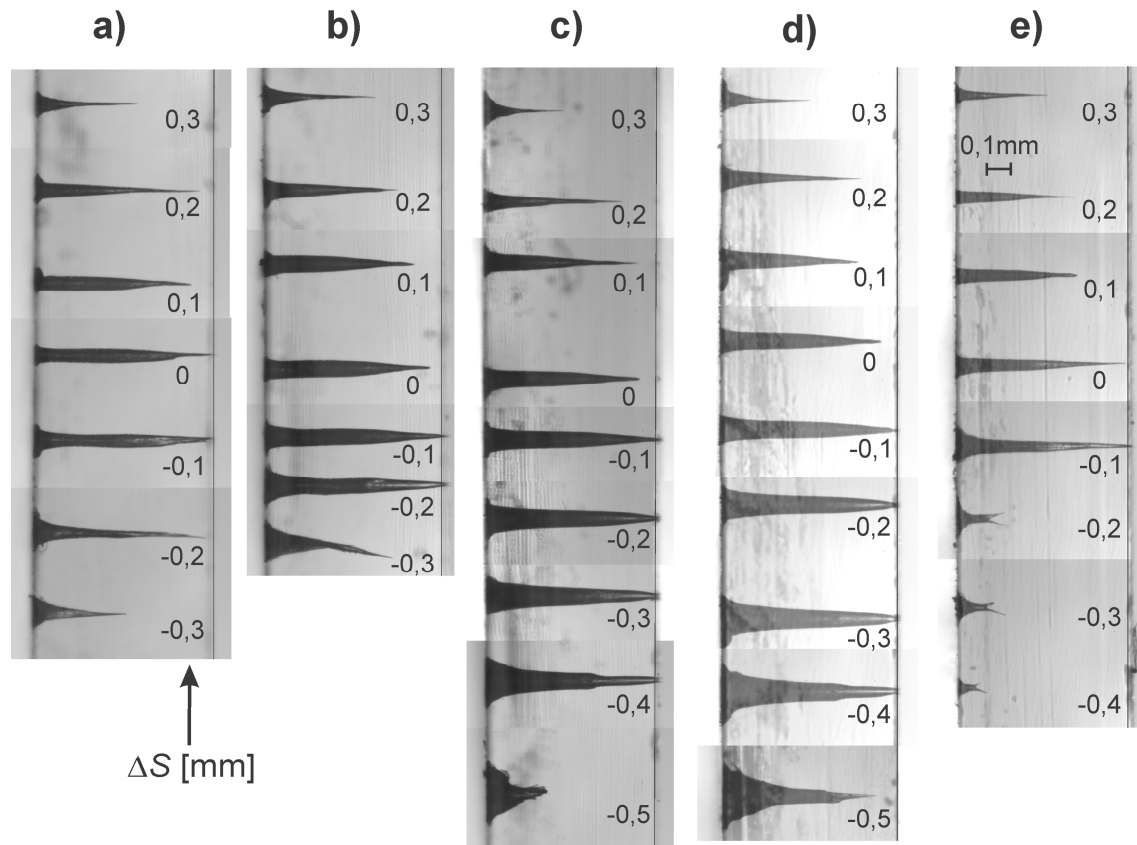


Figure 3. The hole geometry for different processing-beam image-plane positions and typical combinations of pulse-energy and NA values. The image-plane position coincides with the sample surface at the null offset ΔS . The indicated negative image-plane offsets ΔS meet the physical image-plane positions within the glass sample. The image-plane shift ΔS was incremented in 0.1-mm steps. The glass sample thickness was 0.73 mm.

- a) $\varnothing_{O_2} = 7.5$ mm, NA = 0.15, $E_0 = 8.2$ mJ, $E = 0.6$ mJ
- b) $\varnothing_{O_2} = 10$ mm, NA = 0.19, $E_0 = 8.2$ mJ, $E = 1$ mJ
- c) $\varnothing_{O_2} = 15$ mm, NA = 0.29, $E_0 = 8.2$ mJ, $E = 2.3$ mJ
- d) $\varnothing_{O_2} = 20$ mm, NA = 0.38, $E_0 = 8.2$ mJ, $E = 4.1$ mJ
- e) $\varnothing_{O_2} = 20$ mm, NA = 0.38, $E_0 = 4,1$ mJ, $E = 2.1$ mJ

The process passes over to the second phase when the hole shape becomes conical with a small taper angle. Here, a portion of the processing light reflects from the walls and concentrates at the hole tip [10]. For this reason and because of screening by the hole's wall, the plasma starts to expand in one dimension, i.e. in the direction of the hole's longitudinal axis. The ablation is concentrated at the hole tip and a small portion of light energy ablates the wall. The ratio between the tip and wall ablation is defined by the NA and the influence of this ratio on the hole's geometry can be determined from Figure 3. It seems that the tapered shape is more pronounced for high values of NA (Figure 3d) than for low values (Figure 3a), but a more precise description cannot be made because the beam fluences were not equal for all the tests. The hole diameter depends on the beam energy and is almost identical to the focus diameter when this energy approaches the damage threshold value. Employing the unique feature of this phase, i.e. that the removal rate is constant [16, 17, 18], a precise hole depth can be achieved by applying a certain number of laser pulses. With a particular choice of the beam parameters (Figures 3a and 3b) and when the NA is low and the image

plane has been shifted by about 0.1 mm into the bulk material, nearly cylindrical holes can be produced during the second phase with the best aspect ratio and with no effect on the process efficiency. In this case the maximum hole depth is achieved. It is interesting that these findings do not match the theoretical model [1], probably because of the employment of a different test material or different projection system.

The characteristics of the third process phase include sharply tapered holes caused by an increased beam absorption on the side walls of deep holes due to the apex geometry and the presence of re-solidified material. The process terminates when the ablation threshold energy is achieved at the hole's apex. Many beam and material properties define the processing conditions, so drilling results in this phase cannot be precisely predicted. Even small anomalies in the material structure or beam-delivery conditions may lead to unexpected hole geometry such as apex branching (Figure 3e) or a bent apex (Figure 3b). Despite these effects, the hole exit diameter can be as small as a few micrometres when the sample is perforated during the third process phase.

For the evaluation of the holes' geometry we chose a group of characteristic dimensions described in Figure 4. The criterion for the separate phase determination is also seen from the figure. We used the second process-phase dimensions to determine the criteria for the hole-geometry evaluation because the second phase dimension shows the best repeatability.

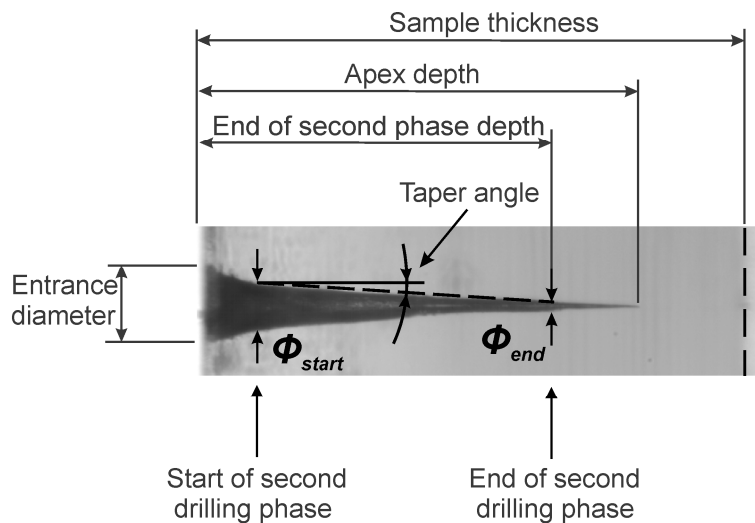


Figure 4. Characteristic dimensions of the hole. Its depth and average diameter are taken from the second drilling-phase geometry

The beam diameter at the image plane ϕ_P can be theoretically predicted using equations of geometrical optics:

$$\phi_P = \frac{\phi_M \cdot F}{S1}, \quad (1)$$

and should be 50 μm wide in our case. Considering the theory of Gaussian beam propagation the approximate beam diameter ϕ_P can be expressed as:

$$\phi_p \approx \frac{2 \cdot \lambda}{\pi \cdot \arctan\left(\frac{\phi_{O2}}{2F}\right)}, \quad (2)$$

where λ is the wavelength of the beam. In the case of the smallest diameter of the aperture ϕ_{O2} , the increase in the beam diameter ϕ_p is the largest and is about 1 μm ; therefore, this effect can be neglected. So the real diameter (60 μm), measured as the diameter of the ablated region after the first laser pulse, is wider mainly due to optical system aberration. To explain this effect, a model of the objective-lenses assembly is used to evaluate the image distortion. Figure 5 shows the calculated intersection of the border rays for various experimental ϕ_{O2} . As has already been mentioned, we located the image plane at the place where the focused beam was the narrowest when the largest O2 aperture was used. This position is marked with the dash vertical line in Figure 5. It should be noted that all the rays between the border ones are omitted from the figure for better clarity, but must be considered for further explanation. When the diameter of the O2 aperture is small, only the rays near the optical axis propagate through the objective and intersect at a certain point, i.e. the theoretical focus. When increasing the O2 diameter the number of marginal rays increases and their intersections move toward the objective, so the real focus of the beam spreads in the same direction. Furthermore, the energy distribution perpendicular to the optical axis becomes non-uniform, with a changeable profile depending on the shift of the observation plane and with higher values of the energy near the optical axes. Another interesting feature can be observed: the divergence of the focused beam in front of the focus is smaller than the divergence on the opposite side.

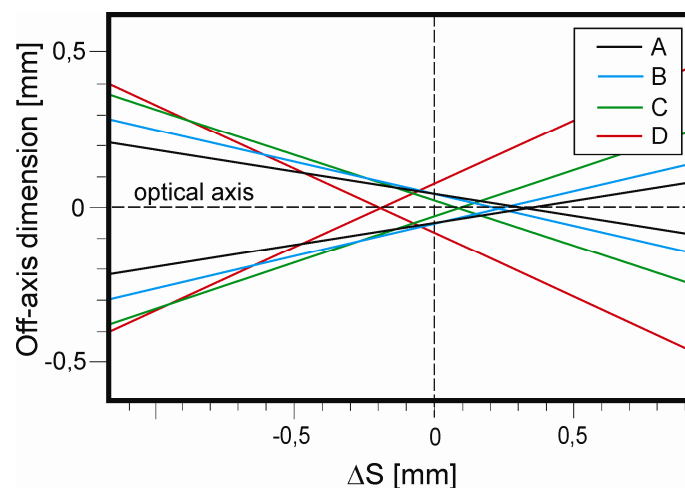


Figure 5. Theoretical ray propagation near the focal point performed by OSLA-EDU software. The lines show the border rays at different O2 diameters:

- A) $\phi_{O2} = 7.5 \text{ mm}$, NA = 0.15
- B) $\phi_{O2} = 10 \text{ mm}$, NA = 0.19
- C) $\phi_{O2} = 15 \text{ mm}$, NA = 0.29
- D) $\phi_{O2} = 20 \text{ mm}$, NA = 0.38

Figure 6 presents the characteristic dimensions of the holes in Figure 3 and graphically demonstrates the influence of a typical pulse-energy/NA combination and the image-plane offset. The

dimensions were determined from photographs of the holes' cross sections (Figure 3), where the plate's thickness (0.73 mm) was taken as the reference dimension. Accordingly, labels A to E in the legend of each figure correspond to the processing beam's properties. Furthermore, the data shown in each diagram at the null image-plane offset were taken from a snapshot marked with $\Delta S = 0$ in Figure 3.

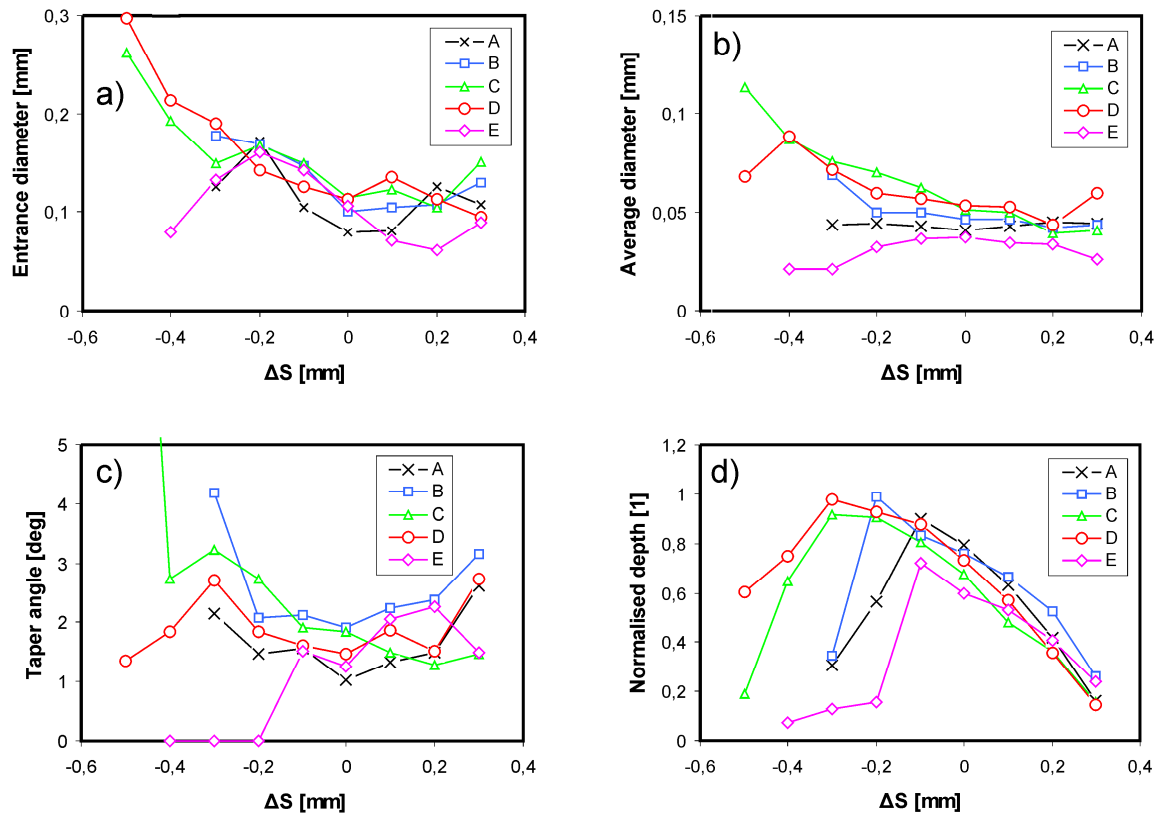


Figure 6. Characteristic dimensions of the holes' dependence on the image-plane offset ΔS . Graphs A to E in all the figures represent the results of different combinations of pulse-energy/NA.

- A) $\varnothing_{O_2}=7.5\text{mm}$, NA=0.15, $E_0=8.2\text{ mJ}$, $E=0.6\text{mJ}$
- B) $\varnothing_{O_2}=10\text{mm}$, NA=0.19, $E_0=8.2\text{ mJ}$, $E=1\text{mJ}$
- C) $\varnothing_{O_2}=15\text{mm}$, NA=0.29, $E_0=8.2\text{ mJ}$, $E=2.3\text{mJ}$
- D) $\varnothing_{O_2}=20\text{mm}$, NA=0.38, $E_0=8.2\text{ mJ}$, $E=4.1\text{mJ}$
- E) $\varnothing_{O_2}=20\text{mm}$, NA=0.38, $E_0=4,1\text{ mJ}$, $E=2.1\text{mJ}$

Figures 6a and 6b present the characteristic hole diameters. Based on the graphs, it can be concluded that the entrance hole diameter (Figure 6a) and the average hole diameter (Figure 6b), the latter being defined by $(\varnothing_{start}+\varnothing_{end})/2$, respond equally to the processing-beam parameters. The figures show the increase in diameter when the image plane is shifted towards the sample, which can be explained by the beam-diameter enlargement on the surface due to its divergence presented in Figure 5. Assuming that each ray contains the same portion of energy, a beam with a nearly uniform fluence profile hits the surface so the entrance-hole diameter corresponds to the beam diameter, i.e. the hole diameter increases with the surface shift. When the image plane is shifted away from the sample surface, the central rays start to concentrate near the optical axis while the marginal rays start to fade with the surface shift. Therefore, the fluence becomes lower approaching the beam's margin.

The effect of plasma shielding also takes place so the hole diameter maintains its minimal value at a null image plane offset. In this case, the hole diameter depends mainly on the beam energy while the image-plane shift is less influential, although the beam diameter increases. Similar behaviour can be noticed for the entrance and average diameters of a hole. Overall, the holes have a smaller diameter than could be expected according to the results of the modelled objective assembly. The reason is probably the energy profile, which is not perfectly uniform. The incident angle of each ray also decreases when the ray travels closer to the optical axis. Both factors decrease the impinging fluence as the rays approach the beam's border. Because of the different plasma formation and consequently the different ablation direction, the entrance-hole diameter, established out of the second-phase hole geometry, is more than two times greater than the average diameter, while the latter is equal to or slightly smaller than the image diameter at the image plane.

Figure 6c shows the change of the taper angle with the image-plane shift for different typical pulse-energy/NA combinations. The variation of the taper angle is almost insensitive to the beam's NA and energy. Only a small increase can be detected when the NA and the corresponding energy are increased and when the image plane is shifted from its central position in both directions. At this point it should be noted that the taper angle was evaluated according to the hole dimensions in the second process phase.

In contrast to the taper-angle behaviour, the hole's depth shows a stronger dependence on the image-plane offset (Figure 6d). Deeper holes can be produced with an image-plane shift into the bulk. A shift in the opposite direction leads to a significant decrease in hole depth. In all cases, the greatest depth is obtained with the image-plane position shifted into the sample by 0.1-0.3 mm. A less than 20% hole-depth reduction occurs when the image plane is located on the sample surface. The normalised hole depths in Figure 6d are defined as a ratio of the depth of a particular hole to the depth of the deepest one.

The third phase hole geometry is not as repeatable as the second phase, so we did not make any further dimensional evaluation. However, the third process phase is very important from the view of applicability. The hole diameter in this phase drastically decreases to a few micrometres and the hole starts to grow in the shape of a capillary. This hole geometry permits only a one-dimensional plasma expansion with a very low transverse dimension and a large longitudinal length. Plasma shielding becomes an increasingly predominant drilling parameter, which leads to a spontaneous termination of the process. The random nature of the plasma-formation phenomena is a key factor for the low geometrical repeatability of the process in its third phase. With the performed drilling tests we confirm that the depth of the third-phase hole cannot be precisely predicted. For that reason, through-hole microdrilling can only be performed with a reliable control of the second-phase hole geometry.

In general, laser-percussion deep microdrilling is characterised by three process phases according to the three different types of plasma-plume formation when the processing beam with a fluence higher than the threshold value is used. The three phases are related to the removal rate or the hole depth versus the laser-pulse number [13, 14].

CONCLUSIONS

We have presented the results of microdrilling in soda-lime glass samples based on a UV excimer laser beam and a modified mask-projection technique. We analysed the effects of the laser

beam's image-plane position shift at different pulse-energy/NA combinations on the hole's geometry. The process consists of three consecutive phases according to the plasma-plume formation. We show that each phase is characterised by the geometrical properties of the holes. The beam geometry has a unique effect for each processing phase, so knowledge of the phase presented during the perforation in combination with the beam's geometrical properties is important for achieving the desired drilling results. The explanation of the hole's diameter dependence on the NA and the image-plane shift can be found by considering the focusing optical system model when holes are drilled within the first and the second drilling-process phases.

The processing image-plane position with respect to the sample's front surface significantly affects the drilling efficiency. Cylindrical holes with the highest aspect ratio and the highest depth were obtained by shifting the image-plane position into the processing sample. It was also shown that the processing beam with a low numerical aperture and energy slightly above the threshold values should be used for processing cylindrically shaped holes with the smallest diameter. Holes with exit diameter up to 10 times smaller than the beam focus diameter were produced in the case where perforation occurs during the third process phase, where the hole tip is in the form of a thin capillary.

REFERENCES

1. V. N. Tokarev, J. Lopez and S. Lazare, "Modelling of high-aspect ratio microdrilling of polymers with UV laser ablation", *Appl. Surf. Sci.*, **2000**, 168, 75-78.
2. B. Keiper, H. Exner, U. Loschner and T. Kuntze, "Drilling of glass by excimer laser mask projection technique", *J. Laser Appl.*, **2000**, 12, 189-193.
3. W. Yuan and B. Ma, "Micro-machinability of monocrystal silicon by direct etching using excimer laser", *J. Mater. Process. Technol.*, **2008**, 200, 390-397.
4. K. H. Gerlach, J. Jersch, K. Dickmann and L. J. Hildenhagen, "Design and performance of an excimer-laser based optical system for high precision microstructuring", *Optics Laser Technol.*, **1998**, 29, 439-447.
5. R. Pini, R. Salimbeni, G. Toci and M. Vannini, "High-quality drilling with copper vapour lasers", *Opt. Quant. Electron.*, **1995**, 27, 1243-1256.
6. R. Petkovšek, A. Babnik and J. Diaci, "Optodynamic monitoring of the laser drilling of through-holes in glass ampoules", *Meas. Sci. Technol.*, **2006**, 17, 1-7.
7. A. Feldman, D. Horowitz and R. M. Waxler, "Mechanisms for self-focusing in optical glasses", *IEEE J. Quant. Electron.*, **1973**, 9, 1054-1061.
8. C. Y. Ho and M. Y. Wen, "Distribution of the intensity absorbed by the keyhole wall in laser processing", *J. Mater. Process. Technol.*, **2004**, 145, 303-310.
9. K. H. Chen, W. Wu, B. H. Chu, C. Y. Chang, J. Lin, S. J. Pearton, D. P. Norton and F. Ren, "UV excimer laser drilled high aspect ratio submicron via hole", *Appl. Surf. Sci.*, **2009**, 256, 183-186.
10. K. H. Chen, W. Wu, B. H. Chu, C. F. Lo, J. Lin, Y. L. Wang, C. Y. Chang, S. J. Pearton and F. Ren, "190 nm excimer laser drilling of glass slices: Dependence of drilling rate and via hole shape on the diameter of the via hole", *J. Vac. Sci. Technol. B*, **2009**, 27, L42-L46.
11. W. S. Lau, T. M. Yue, T. C. Lee and W. B. Lee, "Un-conventional machining of composite materials", *J. Mater. Process. Technol.*, **1995**, 48, 199-205.

12. C. Paterson, A. S. Holmes and R. W. Smith, "Excimer laser ablation of microstructures: A numerical model", *J. Appl. Phys.*, **1999**, 86, 6538-6546.
13. V. N. Tokarev, J. Lopez, S. Lazare and F. Weisbuch, "High-aspect-ratio microdrilling of polymers with UV laser ablation: Experiment with analytical model", *Appl. Phys. A*, **2003**, 76, 385-396.
14. L. Shah, J. Tawney, M. Richardson and K. Richardson, "Self-focusing during femtosecond micromachining of silicate glasses", *IEEE J. Quant. Electron.*, **2004**, 40, 57-68.
15. C. Buerhop, N. Lutz, R. Weismann and G. Tomandl, "Surface treatment of glass and ceramics using XeCl excimer laser radiation", *Glastech. Ber.*, **1993**, 66, 61-67.
16. J. Ihlemann, "Excimer laser ablation of fused silica", *Appl. Surf. Sci.*, **1992**, 54, 193-200.
17. P. E. Dyer, R. J. Farley, R. Giedl and D. M. Karnakis, "Excimer laser ablation of polymers and glasses for grating fabrication", *Appl. Surf. Sci.*, **1996**, 96-98, 537-549.
18. R. Petkovšek, A. Babnik, J. Diaci and J. Možina, "Optodynamic monitoring of laser microdrilling of glass by using a laser probe", *Appl. Phys. A*, **2008**, 93, 141-145.